MATERIALS SCIENCE

Complex dewetting scenarios of ultrathin silicon films for large-scale nanoarchitectures

Meher Naffouti,[1,2] Rainer Backofen,[3] Marco Salvalaglio,[3]* Thomas Bottein,[1] Mario Lodari,[4] Axel Voigt,[3,5] Thomas David,[1] Abdelmalek Benkouider,[1] Ibtissem Fraj,[2] Luc Favre,[1] Antoine Ronda,[1] Isabelle Berbezier,[1] David Grosso,[1] Marco Abbarchi,[1]* Monica Bollani[4]*

Dewetting is a ubiquitous phenomenon in nature; many different thin films of organic and inorganic substances (such as liquids, polymers, metals, and semiconductors) share this shape instability driven by surface tension and mass transport. Via templated solid-state dewetting, we frame complex nanoarchitectures of monocrystalline silicon on insulator with unprecedented precision and reproducibility over large scales. Phase-field simulations reveal the dominant role of surface diffusion as a driving force for dewetting and provide a predictive tool to further engineer this hybrid top-down/bottom-up self-assembly method. Our results demonstrate that patches of thin monocrystalline films of metals and semiconductors share the same dewetting dynamics. We also prove the potential of our method by fabricating nanotransfer molding of metal oxide xerogels on silicon and glass substrates. This method allows the novel possibility of transferring these Si-based patterns on different materials, which do not usually undergo dewetting, offering great potential also for microfluidic or sensing applications.

INTRODUCTION

Surface functionalization with micro- and nanostructures allows for a complete change of the built-in properties of materials, extending their uses in many domains of application, such as electronics, spintronics (*1*), photonics with plasmonic (*2*) and dielectric (*3*) structures, microfluidics (*4*), tribology (*5*), sensing (*6*), and possibly joining multiple functions on the same platform (*7*). To this end, common methods for micro- and nanopatterning usually rely on templates (*8*) or exploit spontaneous pattern formation such as dewetting (*9*). This latter phenomenon is common to many different inorganic and organic compounds, especially when they are in the form of thin films; it has been observed and exploited in solids (*10*, *11*), liquids (*12*, *13*), and polymers (*14*–*16*).

In the framework of micro- and nanoelectronic devices, the dynamics of solid-state dewetting has been extensively investigated in the past 60 years: In analogy with liquid beading over time (*17*), thin solid films of metals and semiconductors break into small islands upon annealing (even at temperatures lower than the inherent melting point). These materials share the same kind of evolution guided by surface diffusion–limited kinetics: The presence of intrinsic defects in the thin layers or of ad hoc created edges is, upon annealing, the starting point of mass transport (*10*, *18*–*20*). In this process, mass is accumulated in a thick, receding rim at the film edges, which, in turn, evolves under the action of other instabilities (for example, fingering, corner instability, and rim pinch-off) (*21*–*23*) and finally breaks into islands featuring a scarce spatial organization and a relatively large size dispersion. The average size and interparticle distance are set by the initial thickness of the layer, which determines the period of the underlying Rayleigh-like instability [for example, for thin Si films of ~12 nm, the diameter of the dewetted particles is about 230 nm, and their distance is ~800 nm (*17*, *24*, *25*)].

Thus, dewetting has been regarded for a long time as a major drawback, de facto limiting the further size reduction of electronic devices. On the other hand, spontaneous dewetting of metals has been efficiently used as a catalyst for the vertical growth of carbon nanotubes and semiconductor nanowires (*26*–*29*). However, for advanced devices in microelectronics and photonics where a high level of control over size, shape, and position of the structures is the major requirement, the intrinsic randomness of the dewetted islands limits the practical exploitation of this method for micro- and nanopatterning.

Improving the level of ordering of metallic islands is possible by patterning the thin films before annealing. This has been thoroughly addressed in the past years, providing excellent control in the formation of simple squared arrays of well-positioned and uniform gold particles. This was shown for films featuring a thickness of 20 to 250 nm and extending more than 10 μm or less (*30*, *31*), determining a patch aspect ratio R larger than 1:80. More recently, Ye and Thompson (*32*–*34*) demonstrated the spectacular formation of extremely complex patterns in their seminal works on monocrystalline nickel and palladium films (~100 nm thick) epitaxially grown on monocrystalline MgO. A full control over the final outcomes of the dewetting was obtained by introducing ad hoc features within the etched patches, thus guiding the dewetting fronts toward precise and reproducible shapes extending more than ~10 μm (being the aspect ratio of the patches R ~ 1:100). These results remained limited to this specific system, and examples of the same quality were never reported in other crystalline layers featuring smaller aspect ratios.

In analogy with metallic films, dewetting of semiconductors patches was recently shown to be capable of achieving good control over islands formation and size homogeneity in simple squared arrays for both Si (*25*, *26*) and Ge (*35*) layers (~10 nm thick with a pitch of about 1 μm; R ~ 1:100 or more) on amorphous SiO_2. However, any attempt of going beyond such a simple scheme for building semiconductor-based complex nanoarchitectures over larger extensions failed, providing puzzling results (*35*–*37*).

Here, we show, for the first time, that ultrathin silicon films on insulator (UT-SOI; 12 nm thick) dewetting can be perfectly controlled to form a variety of monocrystalline nanostructures with high fidelity over hundreds of repetitions and extremely large scales (5 μm) using

[1]Aix-Marseille Université, CNRS, Université de Toulon, IM2NP UMR 7334, 13397 Marseille, France. [2]Laboratoire de Micro-Optoélectronique et Nanostructures, Faculté des Sciences de Monastir Université de Monastir, 5019 Monastir, Tunisia. [3]Institute of Scientific Computing, Technische Universität Dresden, 01062 Dresden, Germany. [4]Istituto di Fotonica e Nanotecnologie–Consiglio Nazionale delle Ricerche, Laboratory for Nanostructure Epitaxy and Spintronics on Silicon,Via Anzani 42, 22100 Como, Italy. [5]Dresden Center for Computational Materials Science, Technische Universität Dresden, 01062 Dresden, Germany.
*Corresponding author. Email: monica.bollani@ifn.cnr.it (M.B.); marco.salvalaglio@tu-dresden.de (M.S.); marco.abbarchi@im2np.fr (M.A.)

electron-beam lithography (EBL) and reactive-ion etching (RIE). The rim evolution can be engineered to deterministically form a plethora of complex nanoarchitectures of connected islands and wires, with fluctuations of the main structural parameters as low as a few percentages. Remarkably, a picogram of flat monocrystalline silicon in a patch featuring an aspect ratio of ~1:400 can be rearranged in monocrystalline three-dimensional (3D) structures over several micrometers, with a precision of a few tens of nanometers. This level of control is at least one order of magnitude better than any previous reports of patterned dewetting of SiGe (*24*, *25*, *27*, *36*, *38*) and, to our knowledge, never shown with a self-assembly technique in semiconductors. The reported process results from surface diffusion–limited kinetics, as proven by the comparison with 3D phase-field (PF) numerical simulations (*39*–*42*). Our modeling approach enables, for the first time, the investigation of the time evolution of patch geometries featuring a very low aspect ratio (up to 1:160) and including small additional features within them. It allows us to assess and understand the mass transport mechanism leading to the morphologies observed in the experiments while precisely describing the intermediate stages of the evolution and the shapes obtained with longer annealing time. We set the limits of the PF approach considered here in modeling real systems by quantifying the comparison between simulations and experiments. The disagreement between them can be as low as a few percentages for simple shapes, whereas it rises up to ~20% for complex shapes at a longer evolution time. A lower disagreement (of about 10%) can be recovered for complex shapes at a long evolution time by lowering the aspect ratio of the simulated layer.

Finally, despite the importance of silicon on insulator for electronic and photonic devices, these complex shapes cannot be easily obtained via self-assembly in other materials relevant for practical applications. Thus, we exploit the complex nanoarchitectures produced via templated dewetting, using them as a master for nanoimprint lithography of thin films of metal oxides obtained via sol-gel dip coating on silicon and silica substrates. We address the cases of SiO_2 (silica) and TiO_2 (titania) xerogels for high-fidelity reproduction of nanostructures (tens of nanometers height and hundreds of nanometers width) over hundreds of repetitions and on large scales in a few fabrication steps while keeping the maximum temperature below 400°C.

RESULTS AND DISCUSSION

In the case of simple patterns, with sides of 4 and 3 μm, annealing for 3 hours is not enough to complete the dewetting (left panels in Fig. 1, A and B, and fig. S2, left): A rim is formed all along the perimeter of the patch showing long protrusion at the corners, where four islands start to form. However, for these sizes (or larger), the dewetting outcome is not stable (Fig. 1, A and B, middle and right): Different shapes can be found and very often, the patches break in randomly arranged islands with a relevant spread of size and shape as visible in optical dark-field microscope images (fig. S2). For smaller simple patterns having side length similar to the period of the underlying instability [~800 nm, as measured on the same UT-SOI in spontaneously dewetted areas (not shown)], the mass in the patch collapses in a single island (Fig. 1, C and D) (*24*, *25*, *36*, *38*). In these trivial, cases the final outcome is extremely stable and reproducible over hundreds of repetitions.

The level of control over the dewetting dynamics can be improved by adding simple features within large patches (5-μm sided squares), such as dashes, crosses, and combinations of them; the case of three holes milled along one diagonal of the patch is shown in Fig. 1F. The mass available within the patch can be rearranged over micrometric distances to form assemblies much more complex than the initially milled shape. Nonetheless, the relevant structural parameters (Fig. 1F) fluctuate only slightly: A statistical investigation of SEM images revealed that the two islands formed at the corners of the patch can be pinned at a distance D = 5210 nm with a fluctuation of only 42 nm (0.8%; Fig. 1G, bottom). Other characteristic lengths such as l, L, and d fluctuate by 8.5, 4, and 1% respectively (Fig. 1G).

In the case of Ni and Pd on crystalline MnO (*32*–*34*) small and large patches evolved coherently in a well-controlled manner; in our work however, the dewetting dynamics of Si on amorphous SiO_2 is perturbed by several sources of disorder limiting its control to trivial topologies and over a few micrometers lengths. In order to highlight these effects we performed high resolution SEM imaging of a simple pattern (Fig. 1E). Whereas in some parts of the patch the dewetting front is flat and coherently evolving towards the center as expected (Fig. 1E, top), in other parts of the patch a kink is visible (Fig. 1E, bottom). These kinks are usually observed in the presence of small and sharp tips (highlighted with white arrows in Fig. 1E), which pin the dewetting front, breaking its symmetry and leading to uncontrolled behaviors. Tips of the same kind were found on the bare SiO_2 surface (Fig. 1E, bottom) and are also present in spontaneously dewetted UT-SOI. This disorder is attributed principally to the intrinsic roughness of the amorphous SiO2 underlying the thin Si layer.

The long lasting lack of the link between metals and semiconductors can be ascribed to the difficulties in manipulating ultrathin semiconductor layers in contrast to more ductile metals. A first macroscopic difference between the two systems relies in the typical thickness of the layers undergoing dewetting: about 10 nm for Si and Ge but exceeding 100 nm for metals. This determines a much shorter period of the natural instability (spontaneously breaking the flat surface) limiting the maximal scales over which the dewetting can be deterministically controlled. Another relevant consequence of the extremely reduced thickness in semiconductors films is their rapid evolution via corner and rim pinch-off instabilities, preventing the formation of connected and elongated structures. Concerning the experimental process, the dewetting of thin Si films is performed in ultrahigh vacuum (~10^{-10} torr) and its evolution is easily jeopardized by any unwanted impurity on the sample surface while metals are annealed in neutral atmosphere (*32*, *33*). Finally, dewetting of Ni and Pd films patches was observed on a crystalline MgO surface, whereas Si and Ge dewetting is performed on amorphous SiO_2. This important factor brings an intrinsic disorder in the system leading to uncontrolled behaviors over large scales and complicates the simple picture of pure surface diffusion-limited kinetics (*70*–*73*).

The versatility and stability of our method are demonstrated by milling arrays of patterns featuring an increasing level of complexity, adding holes (from one to five) and trenches in different positions within the patch (Fig. 2). Complex patterns, including one to five holes or a simple cross (Fig. 2, A-I to A-V and B-I to B-IV), favor the formation of a few islands and wire-like connected structures. More complex designs, including holes and trenches (Fig. 2, B-V and C-I to C-V), produce isolated islands accounting for a faster evolution toward the final state of dewetting.

The features of the dewetting process illustrated in Figs. 1 and 2 can be justified through the surface diffusion–limited kinetics process of

thermally generated adatoms: The material at the film surface flows down the gradient of the local chemical potential μ, which, for isotropic surface energy, is proportional to the local curvature of the surface κ (*18*). The high curvature at the step edges leads to a retraction of the patch and then to the formation of wavy surface profiles, with peaks and valleys evolving in time (*43*). The UT-SOI breaks as the valleys reach a depth equal to the height of the film and rims form. For squared patches, the higher curvature at the corners leads to additional material fluxes, resulting in morphologies with a higher degree of complexity than simple rims (*32*–*34*, *42*). Adding specific features to the initial pattern, such as the holes of Fig. 1F, produces further mass fluxes, which can be designed for tailoring the final morphologies.

To assess the mechanism at play during the experiments discussed above, we performed 3D numerical simulations of the dewetting process by using a PF model (*39*–*41*) assuming pure surface diffusion–limited kinetics. This approach is selected to deal with 3D geometries and complex evolutions involving topological changes. It consists of a conserved evolution of an auxiliary order parameter, φ, set to 1 in the solid and 0 on the outside, with a continuous variation in between. The surface of the solid phase corresponds to the isosurface φ = 0.5.

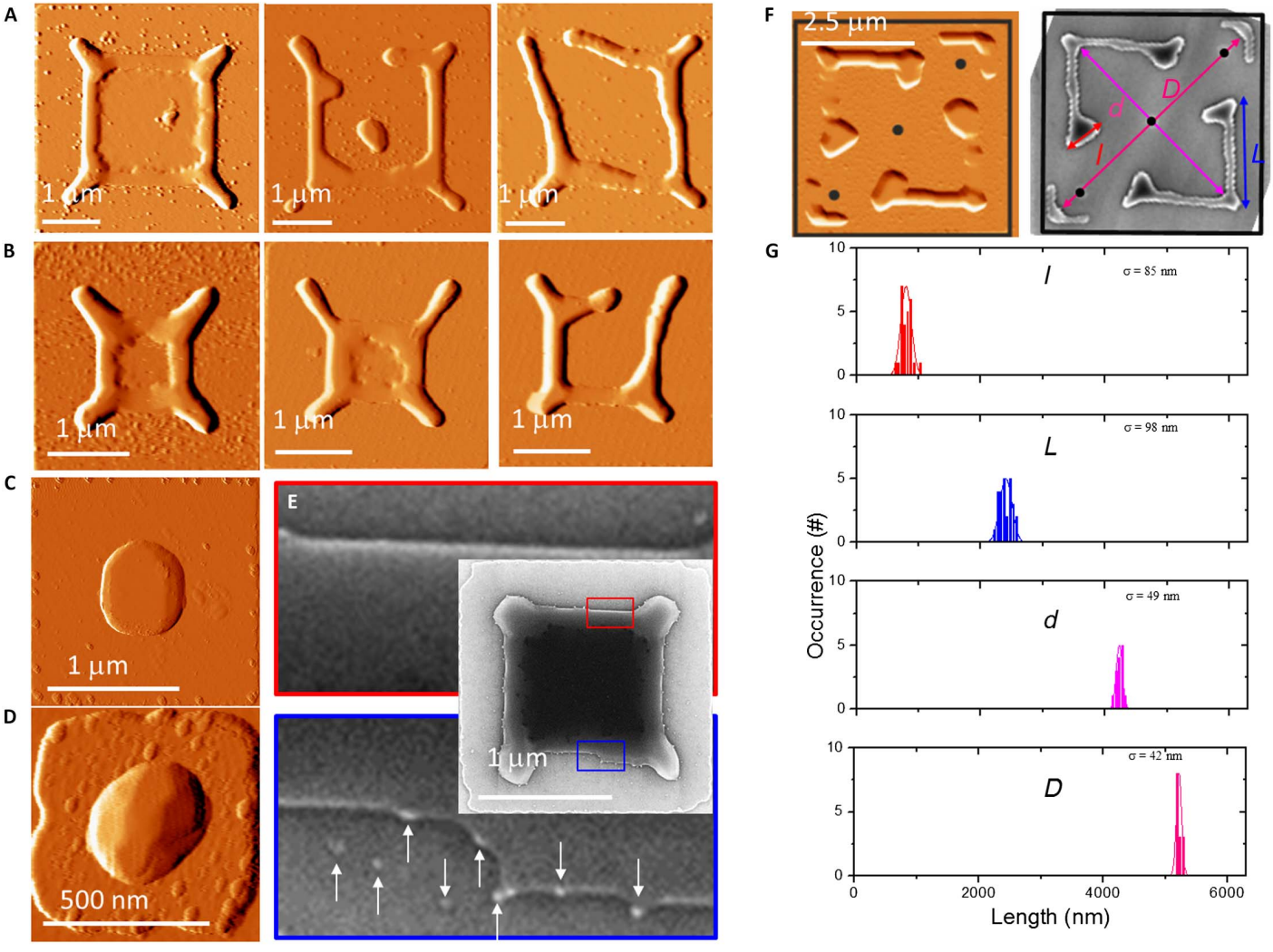

Fig. 1. Dewetting of Si on SiO_2 for simple and complex patterns. (**A**) AFM images of a simple pattern (square having a 4-μm side) annealed for 3 hours. The left panel shows a well-controlled dewetting, whereas the central and right panels show pathologic behaviors where the patch broke in an uncontrolled way. (**B**) Same as (A) for a 3-μm side squared patch. (**C**) AFM image of a simple pattern having a 1.7-μm side annealed for 3 hours. (**D**) Same as (C) for a 600-nm sided simple pattern. Further characterization is provided in fig. S2. (**E**) SEM images of a simple pattern having a 1.7-μm side annealed for 15 min. The center-right inset displays the full pattern. The areas highlighted with a red and blue rectangle are shown in the top and bottom panels, respectively. The top panel displays the case of a flat dewetting front. The bottom panel shows a kink in the dewetting front. Small tips on the patch edge and on the SiO_2 are highlighted by white arrows. (**F**) Left: AFM image of a 5-μm square patch with three holes on the main diagonal annealed for 3 hours (the original shape of the complex pattern is highlighted in black). Right: Same as the left panel for a SEM image. On the SEM, images are highlighted the following distances: *D*, separation of the two islands formed at the patch corners; *d*, separation of the corners of the two large connected structures; *L*, side of the large connected structures; *l*, size of the island forming at the extremity of the large connected structures. (**G**) Statistical distribution of *l* (26 repetitions), *L* (26 repetitions), *d* (14 repetitions), and *D* (14 repetitions) (from the top to the bottom panel, respectively) obtained from SEM images. The corresponding SDs from the average value are reported on each panel. Additional characterization of the islands and size statistical distributions are provided in fig. S4.

For the sake of simplicity, we only focus on isotropic surface energy because it allows us to describe the main features of the process considered here [see also the studies of Jiang *et al.* (*42*) and Salvalaglio *et al.* (*44*)]; for extensions to anisotropic surface energy, see the studies of Torabi *et al.* (*45*) and Salvalaglio *et al.* (*46*)]. In contrast with previous reports of PF modeling of solid-state dewetting (*42*), we adopt here an improved description of the surface diffusion mechanism with a fourth-order polynomial in φ for the mobility function (eq. S2 in the Supplementary Materials) (*47*). Moreover, we adopt a stabilizing function (*40*, *48*) allowing for further numerical improvements (eq. S3 in the Supplementary Materials). The numerical simulations were performed, exploiting the finite element toolbox AMDiS (*49*, *50*) with adaptively refined spatial discretization at the solid-vacuum interface (fig. S5) and an adaptive time-stepping scheme using a Rosenbrock method.

The evolution of a small squared patch with a height-to-base aspect ratio $R = 1{:}40$ (resembling the smallest experimental system as in Fig. 1D, where $R \sim 1{:}41$) is shown in Fig. 3A. The color map illustrates the κ distribution at the surface of the ultrathin silicon on insulator. Slower retraction rate at the corners than at the edges is found, thus forming four protrusions, together with a thinning of the center of the patch. However, the corners finally merge, and a single island is formed in agreement with Fig. 1 (C and D). By halving the aspect ratio *R*, the thinning of the patch leads to the formation of a central hole, whose size increases in time (Fig. 3B). Finally, four elongated ridges connecting the protrusion at the corners are formed (*32*–*34*). Notice that the dynamics of the patch after the formation of the central hole is extremely accelerated with respect to the previous evolution (as also shown in movie S2). The observed morphological differences for aspect ratios $R = 1{:}40$ and $1{:}80$ are in qualitative agreement with previous simulation results shown by Jiang *et al.* (*42*). Notice that despite the different *R* chosen in the experiments (Fig. 1B, where $R \sim 1{:}250$) and in the simulations (Fig. 3B, where $R = 1{:}80$), the intermediate stages in both cases are in agreement. Real structures are expected to show similar qualitative behavior on a larger length scale due to second-order effects such as

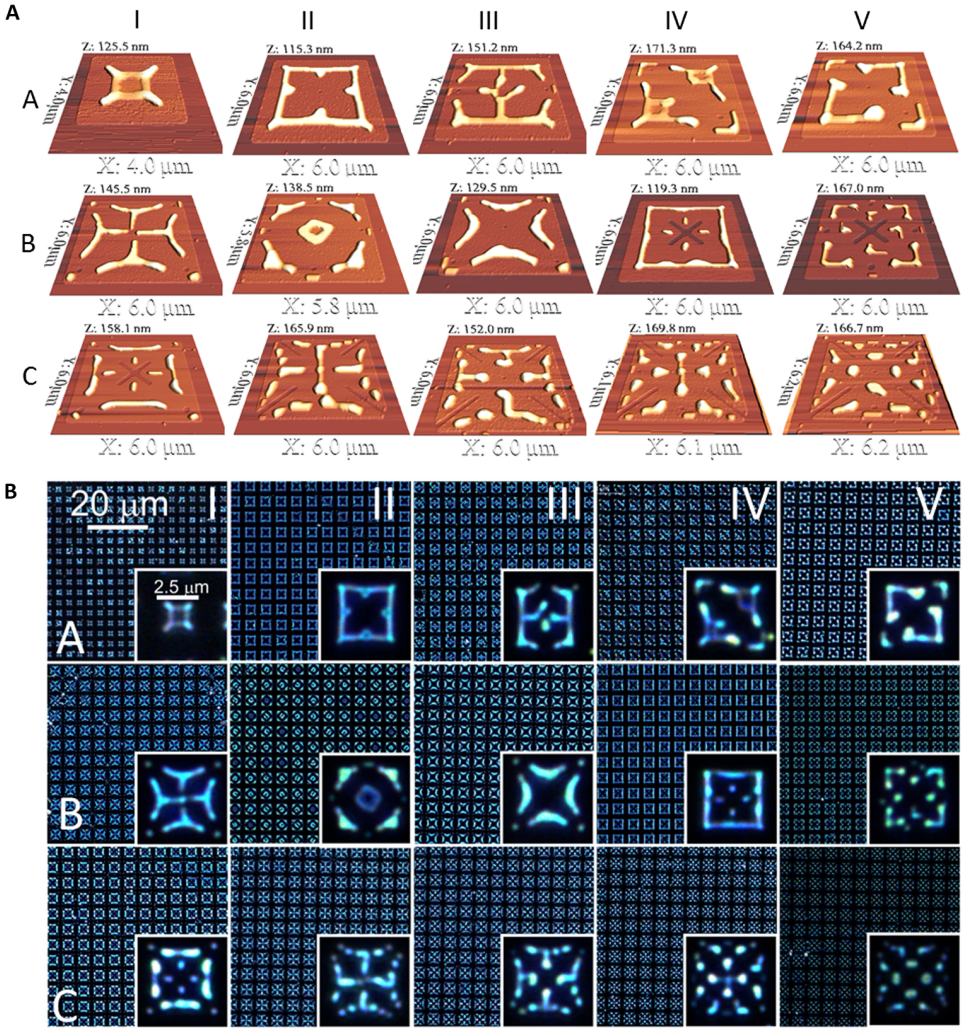

Fig. 2. Structural and optical characterization of dewetted Si on SiO_2. (**A**) 3D view of atomic force microscopy (AFM) images of patches annealed for 3 hours. The corresponding 2D view from the top and the shape of the etched pattern are displayed in the fig. S3. (**B**) Optical dark-field microscopy images. Each panel displays the full patterned area. The bottom right inset in each panel displays an enlarged view of a single dewetted patch. Panels from the top left to the bottom right display patches with an increasing level of complexity of the etched pattern within the main square. The case displayed in A-I corresponds to the PF simulation shown in Fig. 3B (second panel), panel B-I corresponds to Fig. 3C (third panel), panel A-V corresponds to Fig. 3E (fourth panel), and panel B-I corresponds to Fig. 3D (third panel). A quantitative comparison between the experiments and the simulations is provided in Fig. 4.

the orientation-dependent surface energy and diffusivity or the specific wettability conditions of the substrate (*43*).

More complex patch designs are taken into account by keeping R = 1:80 in the simulations (which is almost at the bound for the state-of-the-art feasibility of 3D PF simulations, whereas in the experimental cases, R ~ 1:400; Figs. 2, excluding A-I, and 1F). When adding a small hole in the etched patch, the additional curvature gradients introduced produce a fast depletion of the material from the center (Fig. 2, A-I). Here, the pinning of the ridges occurs earlier with respect to the case of simple square shape (Fig. 3B), and the sides are prevented to move closer to the center. Finally, the rim breaks up in islands further afield than without the initial hole. This mechanism of initiating the depletion of the material and pinning of the crystalline domains between the etched features and the lateral sides is general and is the main tool for controlling the dewetting dynamics. Further examples are provided by the cases of four holes at the corners and of three holes along the diagonal of the patch (Fig. 3, D and E, respectively). In all these cases, the morphologies qualitatively correspond to the experimental outcomes obtained by the dewetting of the patches with similar initial patterning (Fig. 1F and Fig. 2). The good qualitative agreement between the PF simulations and the experiments underlines the key role of surface diffusion in the considered dewetting process. Moreover, it assesses its reproducibility and, in turn, highlights the relevance of our nanofabrication tool and the possibility to choose a priori and ad hoc designs.

To provide more insights and assess further the outcomes of the considered dewetting process, we also discussed the comparison of morphologies obtained in the simulations and experiments during the evolution. In particular, we focus on the two stages obtained by annealing of different durations, namely, short time (ST) and long time (LT). The resulting morphologies of representative cases and the comparison with the corresponding simulations are shown in Fig. 4.

The case corresponding to simple patterns without additional features (as those in Fig. 1C) is illustrated in Fig. 4A. In particular, on the left panels, two scanning electron microscopy (SEM) images show the morphologies obtained for ST and LT, respectively. In the central part of Fig. 4A, their top-view outlines (solid black lines) are compared to the morphologies from the PF simulation of Fig. 3B (dashed blue lines and light blue area), rescaled to match the experimental profiles. To quantify the agreement between these shapes, we evaluated the exclusive disjunction (XOR) of the corresponding areas from the top view and calculated the relative size of the domain where XOR is true (white region in Fig. 4A, right). The percentages reported here are the relative extension of XOR areas with respect to the entire square image. A very good agreement between the experiments and the simulations is found for both stages (XOR smaller than 5%). At later stages, the agreement is extremely good because the system approaches the global equilibrium.

Some cases of complex patterns are shown in Fig. 4 (B to D). In Fig. 4B, the morphologies achieved by dewetting a 1.7-μm squared patch for ST and a 5-μm squared patch for LT with an additional hole at the center are illustrated by SEM images on the left panels, respectively. In the central panels, the outlines of the morphologies from the experiments (solid black lines) and the simulations (dashed red lines and red areas) are also shown. A representative stage of the simulation

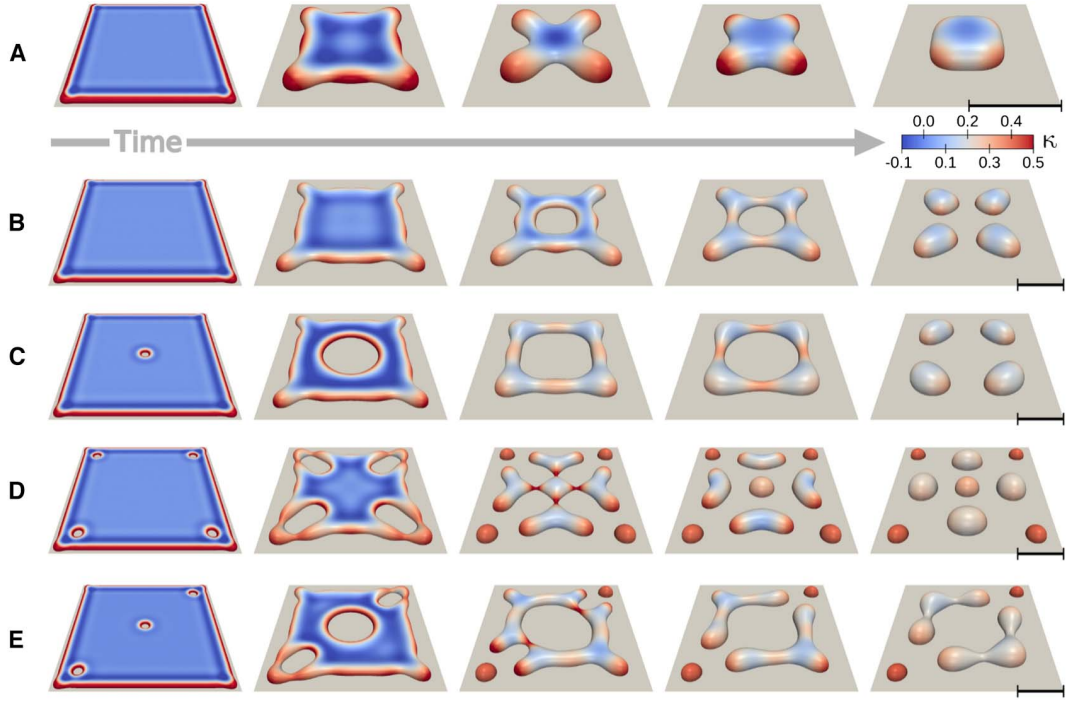

Fig. 3. PF 3D simulations of solid-state dewetting of Si on SiO_2. (**A**) Evolution with time of a squared patch with an aspect ratio of 1:40, corresponding to the experimental setup shown in Fig. 1D. Scale bar, 20 arbitrary units. The color scale represents the local curvature of the surface κ. (**B**) Evolution with time of a simple squared patch with an aspect ratio R = 1:80, leading to the spontaneous formation of a hole at the center. (**C**) Evolution with time of a squared patch with an aspect ratio R = 1:80 with an additional central hole (with a diameter equal to the height of the film), as in Fig. 2 (A-II). (**D**) Evolution with time of a squared patch with an aspect ratio R = 1:80 with four holes at the corners, as in Fig. 2 (B-I). (**E**) Evolution with time of a squared patch with an aspect ratio R = 1:80 with three holes on the diagonal, as in Fig. 2 (A-V). Representative steps of the evolution are selected for each simulation. Complete evolutions, including intermediate stages, can be found in movies S1 to S7. The initial conditions for all the simulations reported here are also shown in the fig. S6.

featuring the same patterning with $R = 1{:}80$ (as in Fig. 3) is selected. The smaller patch is very well reproduced by the simulation (XOR areas, ~7%). The comparison worsens when looking at the larger patch at a long evolution time. However, note that the main features of the final result, including a connected wire-like structure delimiting a square region, are still well described, with a relative XOR area of ~20%. A similar trend is also observed when looking at different stages of a specific patterned patch: The case of three holes along the diagonal is illustrated in Fig. 4C. A relative XOR area of ~10% is achieved for ST, whereas it increases up to ~20% for LT. However, also in this case, the main features of the final structure (topology and positioning of separated islands and elongated domains) are correctly described. From the comparisons shown in Fig. 4 (A to C), we can conclude that using smaller patches with isotropic surface energy allows for a careful evaluation of the symmetry breaking due to the initial patterning because it consists of a purely geometrical effect and is dominant in the early stages (that is, for ST). When considering long time evolutions, the combination of sizes and second-order effects, such as surface-energy anisotropy, is expected to deviate more from the pathway delivered by our simulations. However, we still find a good qualitative agreement under the assumption adopted here. Thus, the reported theoretical results allow for the design of complex morphologies, starting from an initial arbitrary patterning.

When increasing the complexity of the pattern shape, more important deviations are expected. In Fig. 4D, the morphologies at ST and LT of a patch with a central diagonal cross are shown by SEM images on the left panels. The top-view outlines of the morphologies from the experiments (solid black lines) are reported together with the corresponding simulations having $R = 1{:}80$ (dashed red lines and red areas) in the central panels of Fig. 4D (top row). The agreement between the experiments and this simulation is similar to what was observed before with relative XOR areas of ~10% for ST and ~20% for LT. However, here, a crucial feature is missing, that is, the formation of small islands close to the center of the patch. This can be ascribed to the peculiar formation of elongated wires due to the initial cross (as can be seen from the SEM images for ST), which eventually break to form isolated islands

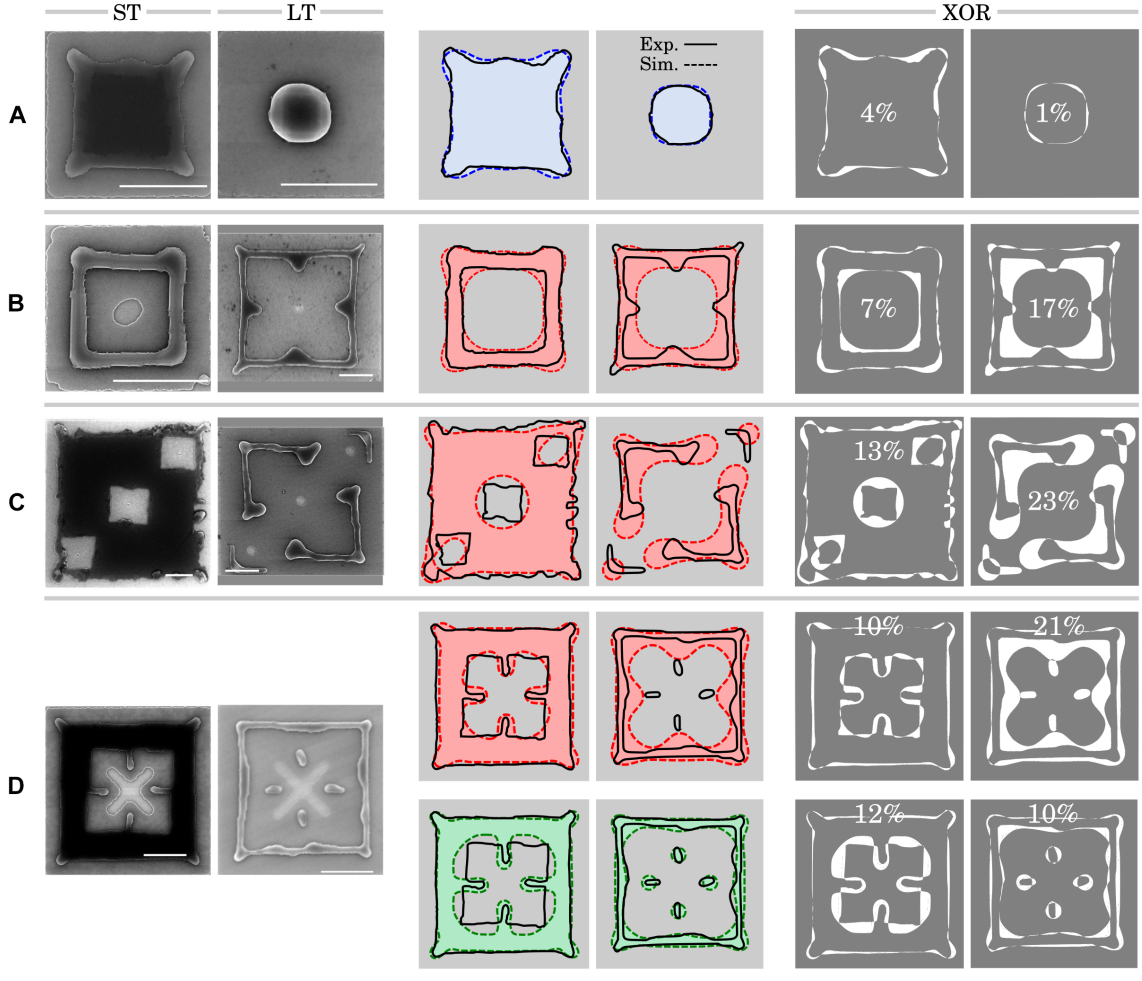

Fig. 4. Time evolution and comparison of dewetting of Si on SiO_2 with PF simulations. For each panel, two SEM images for ST and LT evolution are reported on the left. Scale bars, 1 μm. Superposition of the top-view outline from the experiments (solid black lines) and rescaled PF simulations (dashed colored lines) are shown in the center. The colors of the simulated morphologies correspond to different *R* values: blue, 1:40; red, 1:80; green, 1:160. On the right panels, the XOR area of top-view outlines from the experiments and simulations is shown. The percentages corresponding to the relative XOR area with respect to the total area of the corresponding square image are reported on each subfigure. (**A**) UT-SOI patch, as in Fig. 1C. (**B**) Patch with a hole in the center. Sizes of the patches for the ST and LT cases are 1.7 and 5 μm, respectively. (**C**) Patch with three holes along the diagonal, as in Fig. 1F. (**D**) Patch with a cross in the center, as in Fig. 2 (B-IV). In this panel, the comparisons to two different simulations are shown: top row, $R = 1{:}80$; bottom row, $R = 1{:}160$. The complete evolutions, as obtained by PF simulations, can be found in movies S1 to S7.

at LT. To prove that this detail can also be just ascribed to diffusion-limited kinetics and is mainly related to the design of the initial patterning, we pushed the limit of the computational approach, doubling the initial size of the patch (that is, $R = 1{:}160$). The comparison between the experiments (solid black lines) and this simulation (green dashed lines and green area) is shown in the center of Fig. 4D (bottom row). Here, the size of the simulation allows for the formation of long enough wires that eventually break with the formation of four islands inside the patch. The qualitative agreement with the experiments turns out to improve a lot, and all the main features of the experiments are reproduced. This is confirmed also by the relative XOR area, which is ~10% for both ST and LT morphologies.

These results are the first clear-cut demonstration that, beyond simple squared arrays of individual islands and despite their intrinsic differences, monocrystalline films of metals and semiconductors share the same dewetting dynamics, which is important from a fundamental standpoint. Nonetheless, we achieved this control for extremely large patches featuring an aspect ratio of ~1:400 (to be compared with the

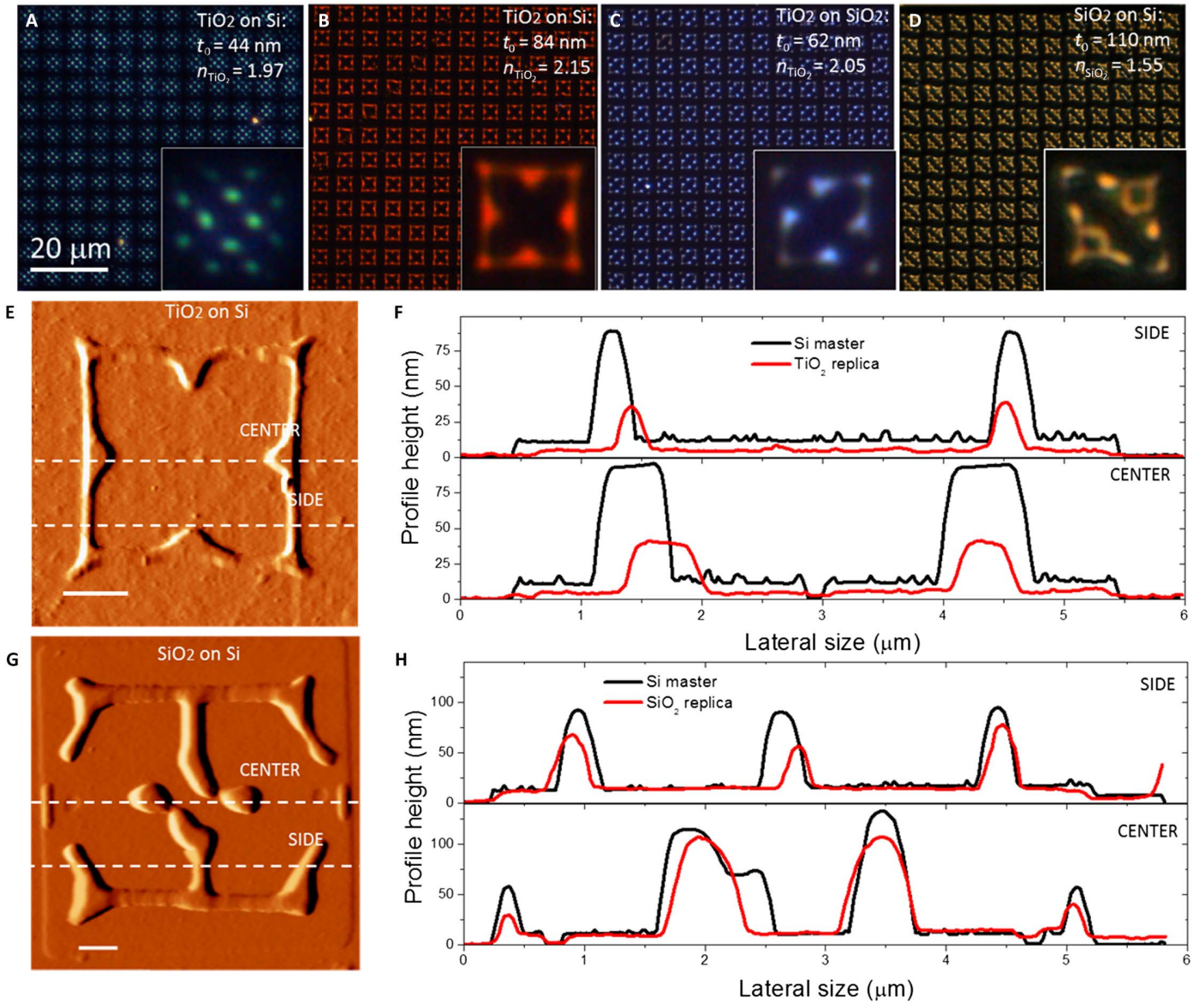

Fig. 5. Nanotransfer molding of titania and silica xerogels on silicon and silica substrates. (**A**) Optical dark-field microscopy image of TiO_2 motif nanoimprinted on a 44-nm-thick xerogel on silicon, reproducing the original silicon master shown in Fig. 2 (C-V). (**B**) Optical dark-field microscopy image of a TiO_2 motif nanoimprinted on 84-nm-thick film, which is a replica of pattern A-II in Fig. 2. (**C**) Optical dark-field microscopy image of TiO_2 motif nanoimprinted on a 62-nm-thick xerogel, replica of the pattern in panel A-V of Fig. 2 printed on a silica substrate. (**D**) Dark-field image of an SiO_2 motif nanoimprinted on a 110-nm-thick xerogel, replica of the pattern A-IV of Fig. 2. On each figure, the material of the nanoimprinted motif, the substrate in use, the initial thickness of the xerogel t_0, and the refractive index of the material after evaporation of the volatile parts are reported. (**E**) AFM image of one individual nanoimprinted TiO_2-based pattern on Si from (B). Scale bar, 1 μm. (**F**) Height profiles "CENTER" (top) and "SIDE" (bottom) extracted from the AFM image in (E) (red lines) and from the corresponding Si master (black lines) shown in Fig. 3 (A-II). (**G**) AFM image of one individual SiO_2-based pattern nanoimprinted on Si from (D). Scale bar, 1 μm. (**H**) Height profiles "CENTER" (top) and "SIDE" (bottom) extracted from the AFM image in (G) (red lines) and from the corresponding Si master (black lines) shown in Fig. 2 (A-II).

case of metals where $R \sim 1{:}100$), showing that this behavior can be predicted via PF simulations. The relevance of these results is also of practical character, given the plethora of uses of nanopatterned silicon. For instance, submicrometer-sized Si and SiGe-based particles obtained via solid-state dewetting can be used as resonant antennas (*25*, *38*). Thus, being capable of framing precise and complex nanoarchitectures starting from simple designs opens the exploitation of this approach for the implementation of dielectric metasurfaces toward exotic optical functionalities (*51*–*54*). The method was extended to amorphous layers of Si (*55*) and SiGe (*38*), showing its importance for submicrometer antennas working at visible and near-infrared frequencies based on different materials (*56*). Provided that the period of instability is set by the initial thickness of the silicon layer, larger or smaller nanoarchitectures can be, in principle, obtained, targeting specific wavelengths ranges. Furthermore, the possibility of tuning the size and shape of the islands and wire-like monocrystalline connected structures, electrically insulated from the substrate, offers a valuable tool for the implementation of ad hoc semiconducting circuits for solid-state memories (*57*). Finally, the integration within the monocrystalline and defect-free silicon-based microcircuits of individual dopants (such as P ions) may represent a step forward in spintronics (*58*).

To extend the range of uses of our nanoarchitectures to other compounds of interest in nanotechnology and on arbitrary substrates, we used the dewetted shapes as a master and transferred them to metal oxide compounds via soft nanoimprinting of thin layers (xerogels) deposited via sol-gel dip coating. The details of the experimental procedure are provided in fig. S7. The mold is obtained in three main steps: first, by passivating the Si-based nanoarchitectures, rendering the master surface hydrophobic; second, by pouring polydimethylsiloxane (PDMS) onto the master; and third, by degassing and annealing at 120°C for 1 hour. The PDMS mold (negative print of the initial substrate) is then peeled off the master surface. Titania and silica xerogel thin films are obtained by dipping and withdrawing (at a constant speed) silicon or glass substrates in liquid solutions containing the precursors. Different withdrawal speeds (between 1 and 6 mm/s) are used to control the initial thickness t_0 of the xerogel. Finally, just after dip-coating, the PDMS mold is placed onto the freshly made xerogel at ambient temperature for 1 min. The xerogel, only partially condensed at ambient temperature, will migrate and fill the PDMS cavities by capillarity. The assembly, composed of xerogel and PDMS, is then annealed at 70°C for 5 min to consolidate the xerogel and peel the mold easily. The metal oxide–based replicas are annealed at 400°C for 30 min to complete condensation and, in the case of titania, to complete crystallization into nanocrystals.

As an example, titania sol-gel coatings are printed with different initial thickness t_0 on silicon and glass wafers. Optical dark-field microscope imaging reveals bright scattering colors (Fig. 5, A to C), which depend on the refractive index of the material, the size and shape of the motifs, and the thickness of a residual underlying, metal oxide layer. The scattered light revealed by dark-field images accounts for the formation of electromagnetic resonances [Mie modes, in analogy with the Si (*25*), SiGe (*38*), and Ge (*56*) counterparts], as recently shown in similar systems (*59*–*64*). These features suggest a straightforward application of our method to dielectric metasurfaces (*51*–*53*).

AFM images show the high fidelity in the reproduction of the complex nanoarchitectures with a vertical and lateral shrinkage of the TiO_2-replicated motifs with respect to the Si master (Fig. 5, E and F). This is a typical consequence of the elimination of the volatile species during drying and thermal annealing of the sol-gel and could be exploited to further reduce the dimensionality of the original structures.

Finally, the same method can be used to swap the composition of the original structures: from Si on SiO_2 on the master to SiO_2 on Si on the replica (Fig. 5D). Here, the lack of a net colorization of the light scattering is attributed to the lower refractive index of the nanoimprinted silica ($n \sim 1.45$) with respect to titania ($n \sim 2$), which does not allow for a large scattering cross section, impeding the formation of Mie resonances (*65*). AFM analysis shows an almost perfect replication with a large reduction of the shrinkage for silica with respect to titania (Fig. 5, G and H). This is expected because silica is amorphous and, at low temperature, is stabilized in a tetragonal coordination sphere, whereas titania instead is crystalline and stabilized in octahedral coordination. This increases the volume of physiosorbed water at a relatively low temperature, resulting in an overall higher shrinkage for titania with respect to silica.

This approach is suitable for the implementation of complex architectures on metal oxide films, which would not be trivial to obtain by other techniques. Moreover, this could be extended to any system compatible with nanoimprint lithography, such as most sol-gels and also polymers. These prototypical examples of metal oxide are relevant for a number of applications in many domains of nanotechnology and have several attractive properties, which are their high chemical, mechanical, and thermal stabilities and their nontoxicity, relative natural abundance, and compatibility with high-throughput sol-gel processing (*66*, *67*). They can be combined with many other components (for example, dispersed plasmonic nanoparticles, quantum dots, lanthanides, etc.) through sol-gel chemistry to tailor their intrinsic built-in properties. Both silica and titania, which have very low absorption at near-ultraviolet frequencies, can be obtained with a controlled porosity, allowing for a precise tuning of their optical constants (*59*). Selective chemical functionalization of silica and titania can be applied in nano/microfluidic channels featuring a tuneable wettability or can be used to add a molecular probe, which is of the utmost importance for applications in sensing (*60*). As for the SiGe-based counterpart, dense titania pillars can be exploited in photonics for dielectric metasurfaces (*61*, *62*, *64*, *68*). Finally, being able to transfer complex patterns on silicon at low temperature is a major requirement for back-end processing of complementary metal oxide semiconductor circuitry and other delicate electronic devices (*69*). This important requirement is met by our nanotransfer process, which is performed at 400°C, thus opening its exploitation on photodetectors, photovoltaic cells, cameras, light-emitting diodes, etc.

CONCLUSIONS

Here, we showed that large silicon patches undergo a complex and ordered self-organization in monocrystalline structures on amorphous SiO_2 when guided by properly engineered dewetting fronts and annealed at high temperature. These features are similar to those found in crystalline Pd and Ni layers on crystalline MnO and are justified in the framework of surface diffusion–limited kinetics. Assuming pure surface diffusion and neglecting any anisotropy during mass transport, PF simulations were optimized to reproduce the evolution in time of the complex shapes formed during dewetting. A detailed comparison between the experiments and the simulations, showing a very good agreement and revealing important insights into both theoretical and experimental aspects, accounts for the predictive character of our modeling approach and opens the way to the implementation of ad hoc Si structures targeting specific shapes and sizes. We exploit the dewetted Si-based patterns as nanoimprint lithography masters for

transferring the complex nanoarchitectures to metal oxide xerogels. This method offers an alternative for nanopatterning different materials, which do not usually undergo dewetting or cannot be easily textured with other techniques. This provides new approaches to dewetting manipulation, showing the potential of our nanoarchitectures as strategic tools for applications in electrically isolated nanocircuits, waveguides, metasurfaces, microfluidic devices, or biomedical sensing.

MATERIALS AND METHODS

A 12-nm-thick UT-SOI was etched with two families of motifs by a combination of EBL and RIE processes: square patches (addressed as simple patterns) having a side length ranging from 600 nm (R ~ 1:41) up to 5 µm (R ~ 1:400) and 5-µm sided squares modified by adding other features within them (for example, pitch, line, cross, etc.; addressed as complex patterns). All the patches were etched along the [110] direction, which constituted the stable dewetting front. Patches oriented along the [100] direction rapidly underwent a fingering instability and broke into isolated islands (not considered in this work).

Two samples were prepared: The first one was annealed in ultrahigh vacuum (~10^{-10} torr) at 720°C for 3 hours (addressed as LT annealing), and the second one was annealed at 740°C only for 15 min @ ~10^{-10} torr (addressed as ST annealing). Note that working at a relatively low temperature (below 750°C) is a necessary requirement to observe the features described below. Larger annealing temperature leads to results of lesser quality in terms of organization and reproducibility of the dewetting outcome.

SUPPLEMENTARY MATERIALS

Supplementary material for this article is available at http://advances.sciencemag.org/cgi/content/full/3/11/eaao1472/DC1

Fabrication and characterization
Simulations
Nanoimprinting
fig. S1. Experimental methods.
fig. S2. Optical and microscopic characterization of simple structures.
fig. S3. Characterization of dewetted structures.
fig. S4. Characterization of the disorder.
fig. S5. PF modeling.
fig. S6. Initial states for dewetting.
fig. S7. Soft nanoimprint lithography process.
fig. S8. Nanoimprinted SiO_2 patterns on a Si substrate.
movie S1. Simple squared patches with R = 1:40.
movie S2. Simple squared patches with AR 1:80.
movie S3. Simple squared patches with R = 1:80 and a central hole.
movie S4. R = 1:80 and four holes.
movie S5. R = 1:80 and three holes on the diagonal.
movie S6. R = 1:80 with cross.
movie S7. R = 1:160 with cross.
References (*74*, *75*)

REFERENCES AND NOTES

1. M. Cavallini, F. Biscarini, J. Gomez-Segura, D. Ruiz, J. Veciana, Multiple length scale patterning of single-molecule magnets. *Nano Lett.* **3**, 1527–1530 (2003).
2. J. A. Schuller, E. S. Barnard, W. Cai, Y. C. Jun, J. S. White, M. L. Brongersma, Plasmonics for extreme light concentration and manipulation. *Nat. Mater.* **9**, 193–204 (2010).
3. S. Jahani, Z. Jacob, All-dielectric metamaterials. *Nat. Nanotechnol.* **11**, 23–26 (2016).
4. H. Andersson, A. V. d. Berg, Microfluidic devices for cellomics: A review. *Sens. Actuators B Chem.* **92**, 315–325 (2003).
5. A. Erdemir, Review of engineered tribological interfaces for improved boundary lubrication. *Tribol. Int.* **38**, 249–256 (2005).
6. F. Xia, L. Jiang, Bio-inspired, smart, multiscale interfacial materials. *Adv. Mater.* **20**, 2842–2858 (2008).
7. M. Cavallini, C. Albonetti, F. Biscarini, Nanopatterning soluble multifunctional materials by unconventional wet lithography. *Adv. Mat.* **21**, 1043–1053 (2009).
8. Y. Lei, S. Yang, M. Wu, G. Wilde, Surface patterning using templates: Concept, properties and device applications. *Chem. Soc. Rev.* **40**, 1247–1258 (2011).
9. D. Quéré, Wetting and roughness. *Annu. Rev. Mater. Res.* **38**, 71–99 (2008).
10. C. V. Thompson, Solid-state dewetting of thin films. *Annu. Rev. Mater. Res.* **42**, 399–434 (2012).
11. J. Lian, L. Wang, X. Sun, Q. Yu, R. C. Ewing, Patterning metallic nanostructures by ion-beam-induced dewetting and rayleigh instability. *Nano Lett.* **6**, 1047–1052 (2006).
12. B. Derby, Inkjet printing of functional and structural materials: Fluid property requirements, feature stability, and resolution. *Annu. Rev. Mater. Res.* **40**, 395–414 (2010).
13. S. Peng D. Lohse, X. Zhang, Spontaneous pattern formation of surface nanodroplets from competitive growth. *ACS Nano* **9**, 11916–11923 (2015).
14. G. Reiter, Dewetting of thin polymer films. *Phys. Rev. Lett.* **68**, 75–78 (1992).
15. R. Xie, A. Karim, J. F. Douglas, C. C. Han, R. A. Weiss, Spinodal dewetting of thin polymer films. *Phys. Rev. Lett.* **81**, 1251–1254 (1998).
16. J. Becker, G. Grün, R. Seemann, H. Mantz, K. Jacobs, K. R. Mecke, R. Blossey, Complex dewetting scenarios captured by thin-film models. *Nat. Mater.* **2**, 59–63 (2003).
17. E. Bussmann, F. Cheynis, F. Leroy, P. Müller, O. Pierre-Louis, Dynamics of solid thin-film dewetting in the silicon-on-insulator system. *New J. Phys.* **13**, 043017 (2011).
18. W. W. Mullins, Theory of thermal grooving. *J. Appl. Phys.* **28**, 333 (1957).
19. O. Pierre-Louis, A. Chame, Y. Saito, Dewetting of ultrathin solid films. *Phys. Rev. Lett.* **103**, 195501 (2009).
20. F. Cheynis, E. Bussmann, F. Leroy, T. Passanante, P. Müller, Dewetting dynamics of silicon-on-insulator thin films. *Phys. Rev. B* **84**, 245439 (2011).
21. M. Dufay, O. Pierre-Louis, Anisotropy and coarsening in the instability of solid dewetting fronts. *Phys. Rev. Lett.* **106**, 105506 (2011).
22. F. Leroy, F. Cheynis, T. Passanante, P. Müller, Dynamics, anisotropy, and stability of silicon-on-insulator dewetting fronts. *Phys. Rev. B* **85**, 195414 (2012).
23. R. V. Zucker, G. H. Kim, W. C. Carter, C. V. Thompson, A model for solid-state dewetting of a fully-faceted thin film. *C. R. Phys.* **14**, 564 (2013).
24. M. Aouassa, I. Berbezier, L. Favre, A. Ronda, M. Bollani, R. Sordan, A. Delobbe, P. Sudraud, Design of free patterns of nanocrystals with ad hoc features via templated dewetting. *App. Phys. Lett.* **101**, 013117 (2012).
25. M. Abbarchi, M. Naffouti, B. Vial, A. Benkouider, L. Lermusiaux, L. Favre, A. Ronda, S. Bidault, I. Berbezier, N. Bonod, Wafer scale formation of monocrystalline silicon-based Mie resonators *via* silicon-on-insulator dewetting. *ACS Nano* **8**, 11181–11190 (2014).
26. X. Duan, C. M. Lieber, General synthesis of compound semiconductor nanowires. *Adv. Mater.* **12**, 298–302 (2000).
27. M. Law, J. Goldberger, P. Yang, Semiconductor nanowires and nanotubes. *Annu. Rev. Mater. Res.* **34**, 83–122 (2004).
28. G. D. Nessim, A. J. Hart, J. S. Kim, D. Acquaviva, J. Oh, C. D. Morgan, M. Seita, J. S. Leib, C. V. Thompson, Tuning of vertically-aligned carbon nanotube diameter and areal density through catalyst pre-treatment. *Nano Lett.* **8**, 3587–3593 (2006).
29. H. J. Fan, P. Werner, M. Zacharias, Semiconductor nanowires: From self-organization to patterned growth. *Small* **2**, 700–717 (2006).
30. A. L. Giermann, C. V. Thompson, Solid-state dewetting for ordered arrays of crystallographically oriented metal particles. *Appl. Phys. Lett.* **86**, 121903 (2005).
31. D. Kim, A. L. Giermann, C. V. Thompson, Solid-state dewetting of patterned thin films. *Appl. Phys. Lett.* **95**, 251903 (2009).
32. J. Ye, C. V. Thompson, Regular pattern formation through the retraction and pinch-off of edges during solid-state dewetting of patterned single crystal films. *Phys. Rev. B* **82**, 193408 (2010).
33. J. Ye, C. V. Thompson, Templated solid-state dewetting to controllably produce complex patterns. *Adv. Mater.* **23**, 1567–1571 (2011).
34. J. Ye, Fabrication of ordered arrays of micro- and nanoscale features with control over their shape and size via templated solid-state dewetting. *Sci. Rep.* **5**, 9823 (2015).
35. A. Karmous, A. Cuenat, A. Ronda, I. Berbezier, S. Atha, R. Hull, Ge dot organization on Si substrates patterned by focused ion beam. *App. Phys. Lett.* **85**, 6401–6403 (2005).
36. M. Trautmann, M. F. Cheynis, F. Leroy, S. Curiotto, O. Pierre-Louis, P. Müller, Dewetting of patterned solid films: Towards a predictive modelling approach. *Appl. Phys. Lett.* **110**, 263105 (2017).
37. N. Meher, T. David, A. Benkouider, L. Favre, A. Ronda, I. Berbezier, S. Bidault, N. Bonod, M. Abbarchi, Fabrication of poly-crystalline Si-based Mie resonators *via* amorphous Si on SiO_2 dewetting. *Nanoscale* **8**, 2844–2849 (2016).
38. T. Wood, M. Naffouti, J. Berthelot, T. David, J.-B. Claude, L. Métayer, A. Delobbe, L. Favre, A. Ronda, I. Berbezier, N. Bonod, M. Abbarchi, All-dielectric color filters using SiGe-based Mie resonator arrays. *ACS Photonics* **4**, 873–883 (2017).
39. J. J. Eggleston, G. B. McFadden, P. W. Voorhees, A phase-field model for highly anisotropic interfacial energy. *Physica D* **150**, 91–103 (2001).

40. A. Rätz, A. Ribalta, A. Voigt, Surface evolution of elastically stressed films under deposition by a diffuse interface model. *J. Comput. Phys.* **214**, 187–208 (2006).
41. B. Li, J. Lowengrub, A. Ratz, A. Voigt, Geometric evolution laws for thin crystalline films: Modeling and numerics. *Commun. Comput. Phys.* **6**, 433–482 (2009).
42. W. Jiang, W. Bao, C. V. Thompson, D. J. Srolovitz, Phase field approach for simulating solid-state dewetting problems. *Acta Mater.* **60**, 5578–5592 (2012).
43. E. Dornel, J.-C. Barbé, F. de Crécy, G. Lacolle, J. Eymery, Surface diffusion dewetting of thin solid films: Numerical method and application to Si/SiO_2. *Phys. Rev. B* **73**, 115427 (2006).
44. M. Salvalaglio, R. Bergamaschini, F. Isa, A. Scaccabarozzi, G. Isella, R. Backofen, A. Voigt, F. Montalenti, G. Capellini, T. Schroeder, H. von Känel, L. Miglio, Engineered coalescence by annealing 3D Ge microstructures into high-quality suspended layers on Si. *ACS Appl. Mater. Interfaces* **7**, 19219–19225 (2015).
45. S. Torabi, J. Lowengrub, A. Voigt, S. Wise, A new phase-field model for strongly anisotropic systems. *Proc. R. Soc. A* **465**, 1337–1359 (2009).
46. M. Salvalaglio, R. Backofen, R. Bergamaschini, F. Montalenti, A. Voigt, Faceting of equilibrium and metastable nanostructures: A phase-field model of surface diffusion tackling realistic shapes. *Cryst. Growth Des.* **15**, 2787–2794 (2015).
47. A. A. Lee, A. Münch, E. Süli, Degenerate mobilities in phase field models are insufficient to capture surface diffusion. *Appl. Phys. Lett.* **107**, 081603 (2015).
48. C. Gugenberger, R. Spatschek, K. Kassner, Comparison of phase-field models for surface diffusion. *Phys. Rev. E* **78**, 016703 (2008).
49. S. Vey, A. Voigt, AMDiS: Adaptive multidimensional simulations. *Comput. Visualization Sci.* **10**, 57 (2007).
50. T. Witkowski, S. Ling, S. Praetorius, A. Voigt, Software concepts and numerical algorithms for a scalable adaptive parallel finite element method. *Adv. Comput. Math.* **41**, 1145–1177 (2015).
51. P. Spinelli, M. A. Verschuuren, A. Polman, Broadband omnidirectional antireflection coating based on subwavelength surface Mie resonators. *Nat. Commun.* **3**, 692 (2012).
52. D. Lin, P. Fan, E. Hasman, M. L. Brongersma, Dielectric gradient metasurface optical elements. *Science* **345**, 298–302 (2014).
53. M. I. Shalaev, J. Sun, A. Tsukernik, A. Pandey, K. Nikolskiy, N. M. Litchinitser, High-efficiency all-dielectric metasurfaces for ultracompact beam manipulation in transmission mode. *Nano Lett.* **15**, 6261–6266 (2015).
54. Y. Yang, W. Wenyi, A. Boulesbaa, I. I. Kravchenko, D. P. Briggs, A. Puretzky, D. Geohegan, J. Valentine, Nonlinear Fano-resonant dielectric metasurfaces. *Nano Lett.* **15**, **7388**–7393 (2015).
55. M. Naffouti, T. David, A. Benkouider, L. Favre, A. Ronda, I. Berbezier, S. Bidault, N. Bonod, M. Abbarchi, Fabrication of poly-crystalline Si-based Mie resonators *via* amorphous Si on SiO_2 dewetting . *Nanoscale* **8**, 2844–2849 (2016).
56. X. Zhu, W. Yan, U. Levy, N. A. Mortensen, A. Kristensen, Resonant laser printing of structural colors on high-index dielectric metasurfaces. *Sci. Adv.* **3**, e1602487 (2017).
57. M. Oehme, A. Karmous, M. Sarlija, J. Werner, E. Kasper, J. Schulze, Ge quantum dot tunneling diode with room temperature negative differential resistance. *Appl. Phys. Lett.* **97**, 012101 (2010).
58. A. Laucht, J. T. Muhonen, F. A. Mohiyaddin, R. Kalra, J. P. Dehollain, S. Freer, F. E. Hudson, M. Veldhorst, R. Rahman, G. Klimeck, K. M. Itoh, D. N. Jamieson, J. C. McCallum, A. S. Dzurak, A. Morello, Electrically controlling single-spin qubits in a continuous microwave field. *Sci. Adv.* **1**, e1500022 (2015).
59. M. Faustini, G. Grenier, G. Naudin, R. Li, D. Grosso, Ultraporous nanocrystalline TiO_2-based films: Synthesis, patterning and application as anti-reflective, self-cleaning, superhydrophilic coatings . *Nanoscale* **7**, 19419–19425 (2015).
60. O. Dalstein, D. R. Ceratti, C. Boissière, D. Grosso, A. Cattoni, M. Faustini, Nanoimprinted, submicrometric, MOF-based 2D photonic structures: Toward easy selective vapors sensing by a smartphone camera. *Adv. Funct. Mater.* **26**, 81–90 (2015).
61. M. Khorasaninejad, W. T. Chen, R. C. Devlin, J. Oh, A. Y. Zhu, F. Capasso, Metalenses at visible wavelengths: Diffraction-limited focusing and subwavelength resolution imaging. *Science* **352**, 1190–1194 (2016).
62. P. Gutruf, C. Zou, W. Withayachumnankul, M. Bhaskaran, S. Sriram, C. Fumeaux, Mechanically tunable dielectric resonator metasurfaces at visible frequencies. *ACS Nano* **10**, 133–141 (2016).
63. C. Zou, P. Gutruf, W. Withayachumnankul, L. Zou, M. Bhaskaran, S. Sriram, C. Fumeaux, Nanoscale TiO_2 dielectric resonator absorbers. *Opt. Lett.* **41**, 3391 (2016).
64. T. Bottein, T. Wood, T. David, J. B. Claude, L. Favre, I. Berbézier, A. Ronda, M. Abbarchi, D. Grosso, "Black" titania coatings composed of sol–gel imprinted Mie resonators arrays. *Adv. Funct. Mater.* **27**, 1604924 (2017).
65. J. van de Groep, A. Polman, Designing dielectric resonators on substrates: Combining magnetic and electric resonances. *Opt. Express* **21**, 26285–26302 (2013).
66. C. Sanchez, C. Boissière, D. Grosso, C. Laberty, L. Nicole, Design, synthesis, and properties of inorganic and hybrid thin films having periodically organized nanoporosity. *Chem. Mater.* **20**, 682–737 (2008).
67. B. Louis, K. Natacha, M. Marco, D. Grosso, Understanding crystallization of anatase into binary SiO_2/TiO_2 sol–gel optical thin films: An in situ thermal ellipsometry analysis. *J. Phys. Chem. C* **115**, 3115–3122 (2011).
68. P. Spinelli, B. Macco, M. A. Verschuuren, W. M. M. Kessels, A. Polman, Al_2O_3/TiO_2 nano-pattern antireflection coating with ultralow surface recombination . *Appl. Phys. Lett.* **102**, 233902 (2013).
69. Y. H. D. Lee, M. Lipson, Back-end deposited silicon photonics for monolithic integration on CMOS. *IEEE J. Sel. Top. Quantum Electron.* **19**, 8200207 (2013).
70. D. J. Srolovitz, S. A. Safran, Capillary instabilities in thin films. I. Energetics . *J. Appl. Phys.* **60**, 247–254 (1986).
71. D. J. Srolovitz, S. A. Safran, Capillary instabilities in thin films. II. Kinetics. *J. Appl. Phys.* **60**, 255–260 (1986).
72. J. W. Cahn, J. E. Taylor, Overview no. 113 surface motion by surface diffusion. *Acta Metall. Mater.* **42**, 1045–1063 (1994).
73. W. C. Carter, A. R. Roosen, J. W. Cahn, J. E. Taylor, Shape evolution by surface diffusion and surface attachment limited kinetics on completely faceted surfaces. *Acta Metall. Mater.* **43**, 4309–4323 (1995).
74. V. Mondiali, M. Lodari, M. Borriello, D. Chrastina, M. Bollani, Top–down SiGe nanostructures on Ge membranes realized by e-beam lithography and wet etching. *Microelecton. Eng.* **153**, 88–91 (2016).
75. J. W. Cahn, C. M. Elliot, A. Novick-Cohen, The Cahn–Hilliard equation with a concentration dependent mobility: Motion by minus the Laplacian of the mean curvature. *Eur. J. Appl. Math.* **7**, 287–301 (1996).

Acknowledgments: We thank D. Chatain, R. V. Zucker, and R. Bergamaschini for the discussions about the experimental results and theoretical PF simulations and V. Mondiali for the useful discussions on EBL and nanoimprinting fabrications. **Funding:** We acknowledge the projects PHC Maghreb (no. 32595SL), EMMAG-Erasmus Mundus Maghreb and Egypte, the Nanotecmat Platform of the IM2NP Institute of Marseille, and the CP2M microscopy center of the Aix-Marseille University for the availability of the tools and the equipment needed for this study. M.S. acknowledges the support of the Postdoctoral Research Fellowship awarded by the Alexander von Humboldt Foundation. The computational resources for PF simulations were provided by Zentrum für Informationsdienste und Hochleistungsrechnen at Technische Universität Dresden and by the Jülich Supercomputing Centre within the project no. HDR06. **Author contributions:** M.N., T.B., T.D., A.B., I.F., L.F., A.R., I.B., D.G., and M.A. performed the dewetting processes, sample structural characterization, and nanoimprinting processes. M.L. and M.B. took charge of the EBL fabrication and SEM characterizations. R.B., A.V., and M.S. were responsible for the PF simulations. M.B, M.A., and M.S. devised the initial concepts and theory and wrote the manuscript. **Competing interests:** The authors declare that they have no competing interests. **Data and materials availability:** All data needed to evaluate the conclusions in the paper are present in the paper and/or the Supplementary Materials. Additional data related to this paper may be requested from M.B. (monica.bollani@ifn.cnr.it).

Submitted 19 June 2017
Accepted 28 September 2017
Published 10 November 2017
10.1126/sciadv.aao1472

Citation: M. Naffouti, R. Backofen, M. Salvalaglio, T. Bottein, M. Lodari, A. Voigt, T. David, A. Benkouider, I. Fraj, L. Favre, A. Ronda, I. Berbezier, D. Grosso, M. Abbarchi, M. Bollani, Complex dewetting scenarios of ultrathin silicon films for large-scale nanoarchitectures. *Sci. Adv.* **3**, eaao1472 (2017).